Metallic Nanoparticle Arrays: A Common Substrate for Both Surface-Enhanced Raman Scattering and Surface-Enhanced Infrared Absorption

Fei Le,[†] Daniel W. Brandl,[†] Yaroslav A. Urzhumov,[‡] Hui Wang,[§] Janardan Kundu,[§] Naomi J. Halas,[§,⊥] Javier Aizpurua,[∥] and Peter Nordlander[†,⊥,*]

[†]Department of Physics and Astronomy, M.S. 61, Rice University Houston, Texas 77005, [‡]Department of Physics, The University of Texas, Austin, Texas 78712, [§]Department of Chemistry, M.S. 60, Rice University, Houston Texas 77005, [⊥]Department of Electrical and Computer Engineering, M.S. 366, Rice University, Houston, Texas 77005, and [∥]Donostia International Physics Center (DIPC) and Centro de Física de Materiales CSIC-UPV/EHU, Paseo Manuel Lardizabal 4, Donostia-San Sebastian 20018, Spain

ABSTRACT Nanoshell arrays have recently been found to possess ideal properties as a substrate for combining surface enhanced raman scattering (SERS) and surface enhanced infrared absorption (SEIRA) spectroscopies, with large field enhancements at the same spatial locations on the structure. For small interparticle distances, the multipolar plasmon resonances of individual nanoshells hybridize and form red-shifted bands, a relatively narrow band in the near-infrared (NIR) originating from quadrupolar nanoshell resonances enhancing SERS, and a very broadband in the mid-infrared (MIR) arising from dipolar resonances enhancing SEIRA. The large field enhancements in the MIR and at longer wavelengths are due to the lightning-rod effect and are well described with an electrostatic model.

KEYWORDS: nanoshell · SERS · SEIRA · plasmonics · surface enhanced spectroscopy · plasmon hybridization

An important application in the emerging field of plasmonics is the development of substrates capable of providing large electromagnetic enhancements, also known as "hot spots", for surface-enhanced spectroscopies (SES).[1–6] The resonant excitation of plasmons in metallic nanostructures can provide large field enhancements on the surfaces of metals,[7–10] which in turn provide dramatic increases in the detected spectroscopic signals for molecules adsorbed on their surfaces. The most widely used SES is surface enhanced raman scattering (SERS), where the electromagnetic enhancement factor is proportional to the fourth power of the field incident on the molecule.[11–14] Recently there has been a resurgence of interest in another type of SES, surface enhanced infrared absorption (SEIRA).[15–23] Even though the electromagnetic enhancement in SEIRA is only proportional to the square of the electromagnetic field, SEIRA is likely to play an increasingly important role in the field of chemical and biological sensing since it probes dipole-active vibrational modes, providing a complementary vibrational analysis of analyte molecules.

One primary reason why SEIRA has received so much less attention than SERS has been the limitations in designing and fabricating nanostructures with reproducible tunable plasmon resonances across the broad infrared (IR) region of the spectrum utilized in this spectroscopy. The maximum electromagnetic enhancement in a plasmonic nanostructure occurs for resonant excitations of the plasmons, which are typically found in the visible and UV regions of the spectrum. However, the plasmon resonances of metallic nanoparticles are strongly dependent on structure and composition.[24–35] This tunability has been very important in recent advances in SERS substrates where substrates consisting of plasmonic nanostructures with resonances overlapping the frequency bands of common laser sources in the visible and near-IR range have been developed.[36]

It has recently been shown that a two-dimensional (2D) hexagonal close-packed (HCP) array of nanoshells with nanoscale gaps between nanoparticles provides significant enhancements to both SERS and SEIRA, effectively combining both spectroscopies on a single substrate.[37] The analysis of the SEIRA signal strengths for paramercaptonaniline (pMA) monolayers deposited on these arrays suggests enhancement factors between 10^3 to 10^5.

*Address correspondence to nordland@rice.edu.

Received for review January 24, 2008 and accepted March 03, 2008.

10.1021/nn800047e CCC: $40.75

Such large values indicate that the dominant enhancement mechanism is electromagnetic rather than chemical in nature. The surprising discovery in this experiment is that the same substrate can provide strong electromagnetic enhancements at the same spatial locations in both the near-infrared (NIR) and the mid-infrared (MIR) regions of the spectrum. The extinction spectra of the arrays were found to be characterized by two features, a relatively sharp resonance in the NIR and a very broad, continuum-like resonance in the MIR. Strong electromagnetic field enhancements are not surprising for excitations of sharp plasmon resonances and can be understood as the resonant pumping of the plasmon as a harmonic oscillator. However, it is quite surprising and not immediately clear what physical mechanism underlies the enhancements associated with the extremely broad MIR feature, with its overdamped oscillator behavior. The primary purpose of this paper is to elucidate and understand the unique characteristics of this array structure, in light of its remarkable electromagnetic enhancement properties.

In this paper the optical and electromagnetic properties of 2D HCP nanoshell arrays on substrates are analyzed using a variety of computational and analytical approaches. We show that the NIR resonance in the 2D HCP nanoshell arrays is formed by interactions of the quadrupolar resonances of the individual nanoshells in a manner directly analogous to the formation of a d-band from the atomic d-orbitals of a transition metal. The hybridized NIR mode is only weakly red-shifted from the quadrupolar nanoshell plasmon because of the relatively weak interparticle coupling of the quadrupolar modes. Plasmon hybridization, however, does not by itself account for the broad MIR spectral features and large local fields that give rise to the observed SEIRA enhancements. The broad MIR resonance is identified as a superradiant hybridized mode originating from the dipolar plasmon resonances of the individual nanoshells, whose much stronger redshift relative to that of the NIR resonance is due to the much stronger interparticle interactions of the dipolar plasmons. Superradiance, the coherent coupling between adjacent resonant systems that results in enhanced radiative damping, is responsible for the extreme broadening of the dipole-derived MIR plasmon resonance in nanoshell arrays. The large field enhancements induced within the MIR resonance envelope are caused by the "lightning-rod" effect, which occurs when metals act as perfect conductors and expel the electric field from the interior of the metals. This screening squeezes the electric field into the junctions between the nanoshells, resulting in large field intensities. We show that for metallic arrays, the lightning-rod effect can be described semianalytically for arrays of arbitrarily shaped nanoparticles using an electrostatic model. Our analysis reveals a universal inverse linear relation between the maximum electric field enhancement and the lattice constant, a parameter that is independent of the shape of the particle. To describe the relevance of the field enhancements for SEIRA, we introduce the concept of hotspot volume. The hotspot volume is defined as the volume within which the electric field enhancements are larger than half of the maximum field enhancement. We show that this quantity depends strongly on the shape of the particles that constitute the SEIRA array substrate.

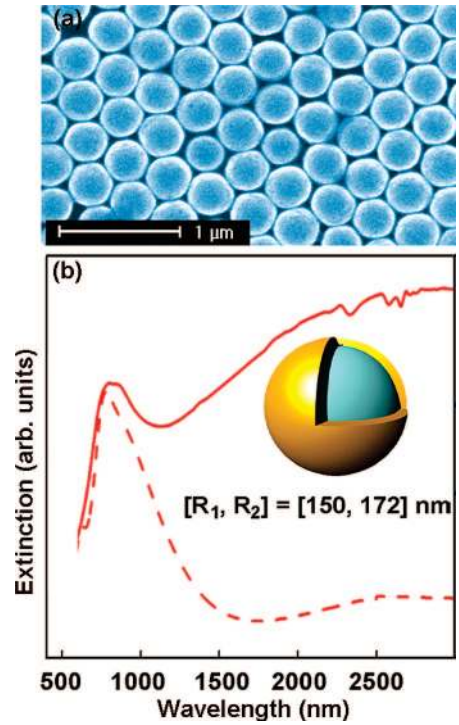

Figure 1. SEM image and extinction spectra of a typical HCP Au nanoshell array sample. Panel a shows an SEM image of the sample. The inner radius of the nanoshells is 150 ± 12 nm and the gold shell thickness is 22 ± 1 nm. The separation *d* between adjacent nanoshells is nominally 8 nm. Panel b shows the normal incidence extinction spectrum of the array (solid) and that of an isolated nanoshell with the same size (dashed).

RESULTS AND DISCUSSION

Experimental Spectra of Nanoshell Arrays. In Figure 1a, an SEM image of a typical nanoshell array with nanoscale gaps between adjacent nanoparticles is shown.[37] The geometry of the nanoshells is $(r_1, r_2) = (150, 172)$ nm, where r_1 and r_2 are the inner and outer radius of the nanoshell, respectively. The separation between adjacent nanoshells is $d = 8$ nm, determined by the thickness of the double layer of cetyltrimethylammonium bromide (CTAB) molecules in the junction, which serves as a molecular spacer layer, preserving interparticle gap distances during array self-assembly. The extinction spectrum of the array and of an individual nanoshell of the same size as the array-constituent nanoparticles is shown in Figure 1b. For an individual nanoshell of these dimensions, the dipolar peak occurs at nominally 900 nm and the quadrupolar peak at 700

nm. The small shoulder at 2500 nm in the individual nanoshell spectrum is due to the presence of a few small nanoshell dimers and aggregates along with the individual, isolated nanoshells. For the nanoshell arrays, a short wavelength feature merges into a strong and broad resonance that extends well into the MIR. This broad spectral feature is cut off at 3000 nm owing to the wavelength limit of the spectrometer. Although the resonance is just beginning to level off at nominally 3000 nm, for convenience we will refer to this feature as the 3000 nm MIR resonance.

FDTD Simulations. To model the HCP nanoshell array, we use the FDTD method with periodic boundary conditions (PBC).[38] The implementation of PBC is straightforward for normal incidence illumination. A Drude dielectric function is used to describe the optical response of gold, with parameters fit to experimental data.[39] We are able to computationally model rectangular unit cells with sizes of approximately 500 nm^3, so in principle we could also include a dielectric substrate with a thickness of a few hundred nanometers, if needed. However, for normal incidence, the major effect of such a substrate is a uniform 50–150 nm redshift of all the spectral features of the array. In addition, for short wavelengths the simulated spectra would display thickness-dependent modulations caused by Fabry–Perot resonances in the substrate, which would not be present for the experimental substrates, which were a few millimeters thick. Since including a dielectric substrate would have little effect on the array properties we are studying, a substrate is not included in our calculations.

In Figure 2 the calculated FDTD-PBC spectra and local electric field enhancements for the HCP nanoshell array of Figure 1 are shown. The absorption, scattering, and extinction spectra are calculated. The theoretical extinction spectrum shows a narrow resonance at an energy of around 750 nm and a remarkably broad feature beginning around 1000 nm and extending far into MIR well beyond the graph cutoff at 3000 nm. We also see that the low-energy (long wavelength) broad feature in the extinction spectrum is dominated by scattering. Since the metal becomes a better conductor at longer wavelengths, electromagnetic fields are excluded from the array in the long wavelength limit, limiting MIR absorption. The local electromagnetic field enhancements induced at $\lambda = 700$ nm (Figure 2b) and $\lambda = 3000$ nm (Figure 2c) are displayed. The field enhancement is defined as the ratio of the electric field amplitude at a given position to the incident field value in the absence of the nanostructure. In Figure 2b, the near-IR enhancements appear as relatively small local field hot spots between neighboring nanoshells with a maximum field enhancement = 12.9 and small enhancement factors inside each nanoshell. Figure 2c shows MIR hot spots at the same spatial location as the NIR hot spots, but with a somewhat greater spatial extent and a larger maximum field enhancement factor of 19.1.

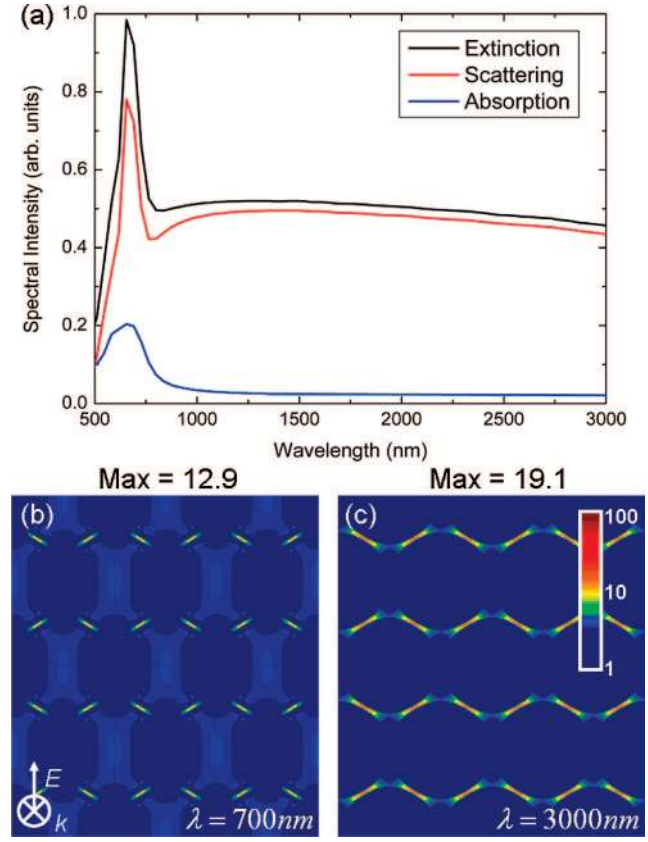

Figure 2. FDTD simulation results for an HCP Au nanoshell array. The geometry of the nanoshell is (r_1, r_2) = (150,172) nm, the separation is d = 8 nm, and the grid size is 2 nm. The periodic unit cell is composed of four half-nanoshells. Panel a shows the extinction (black), scattering (red), and absorption (blue). Panels b,c show the local electromagnetic field enhancements at wavelengths of 700 and 3000 nm, respectively.

Lineshape of the MIR Resonance. While the energy and line shape of the NIR resonances of the calculated spectra shown in Figure 2 agree nicely with the experimental data of Figure 1, the low-energy (long wavelength) features clearly differ. The experimental spectrum shows a broad shoulder that appears to peak at approximately 3000 nm, while FDTD calculations show a uniform, constant amplitude feature for wavelengths above 1000 nm. To examine this discrepancy, we investigated how the structural parameters of the array influence the resonances in the extinction spectrum. Varying the array separation, d, from 6 to 500 nm results in a blueshift and narrowing of the low-energy (long wavelength) continuum, and ultimately transforms the array spectrum into an individual nanoshell spectrum in the large particle separation limit. With this approach, we were never able to reproduce the strong MIR extinction maximum at 3000 nm observed experimentally. We also examined the effects of dielectric screening mediated by the CTAB layers around each nanoshell. Screening effects are negligible on the array extinction spectrum, but the maximum field enhancements are in-

creased by 5–10% . We also performed calculations investigating effects due to the glass substrate, but again, the low-energy (long wavelength) feature remained a broad structureless continuum. We conclude that the broad, featureless MIR peak of Figure 2a is a manifestation of superradiant behavior, in other words, a collective enhancement of the dipolar radiation and radiative damping of interacting, coherently oscillating dipoles within a spatial volume smaller than the wavelength of incident light.[40] Such behavior has been seen in other collections of dense resonant systems, such as Bose−Einstein condensates,[41] semiconductor nanoparticle aggregates,[42] even the background emission of rotating black holes.[43] Recently, subradiant and superradiant coupling in plasmonic crystals has been reported.[44,45] In our case, the discrepancy observed between the broad, flat MIR feature obtained theoretically and the 3000 nm peak seen in the experimental array spectrum is due to inhomogeneities in the experimental sample which arise from a dispersion in nanoshell sizes and the resultant variations in interparticle spacings. If these imperfections in the nanoshell arrays were removed or minimized, the line shape of the 3000 nm MIR feature should indeed broaden in agreement with the theoretically predicted spectrum for the array.

Plasmonic Properties of Nanoparticle Clusters. To gain more insight into the microscopic nature of the plasmons in HCP nanoshell arrays, we calculated the extinction spectrum of an individual nanoshell, a symmetric nanoshell trimer, and a symmetric nanoshell septamer (one nanoshell in the center and six nanoshells symmetrically distributed around it in the same plane). In Figure 3 we compare the normalized extinction spectra of these finite systems with that of the nanoshell array constructed from nanoshells of the same geometry. The finite structures were modeled using the same interparticle spacings as in the array. Mie theory analysis for the individual nanoshell shows a dipolar resonance around 1000 nm, a quadrupolar around 750 nm, and a weak octupolar resonance around 600 nm. In all four spectra, the sharp peaks at 750 nm overlap identically. From this observation we can conclude that this spectral feature originates from the quadrupolar plasmon resonances of the individual nanoshells. The reason for the very weak shift of the quadrupolar resonance with increased coordination is the weak interaction and hybridization of quadrupolar modes in adjacent nanoparticles.[46] The low-energy (long wavelength) resonances in Figure 3, on the other hand, follow a clear trend of redshifting and broadening with increasing coordination. The individual dipolar nanoshell resonance at 1000 nm shifts to 1500 nm for a nanoshell trimer and to 2000 nm for the lowest energy nanoshell septamer resonance. The line shape of the septamer spectrum is characterized by a broad peak centered at 2000 nm with a much narrower, asymmetric dip in the

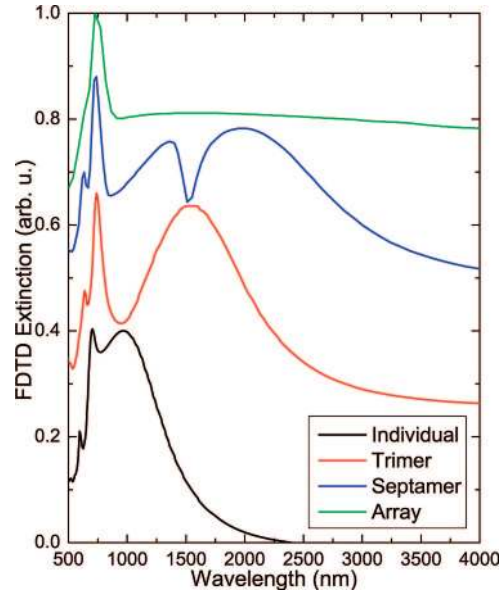

Figure 3. FDTD extinction spectra of an individual nanoshell (black), a nanoshell trimer (red), a nanoshell septamer (blue), and a HCP nanoshell array (green). The geometry of the nanoshells is (r_1, r_2) = (150,172) nm, and the separation is d = 8 nm. The quadrupolar modes of these structures are all located around 700 nm. The dipolar peaks show a strong redshift with increasing number of neighboring nanoshells.

extinction spectrum located around 1500 nm. This Fano-type profile arises from an interference between the narrow (subradiant) and broad (superradiant) plasmon modes of the nanoshell septamer. This is similar to recently discussed Fano lineshapes observed in coupled multilayer plasmonic wires.[45]

Fano Resonance. The modal interference that gives rise to the Fano-type resonance in the nanoshell septamer spectrum is clearly illustrated in Figure 4, where the local electromagnetic field enhancements for wavelengths around the dip are shown. For the subradiant mode on the short wavelength side of the dip, the largest fields occur in the junctions between the six particles that surround the central nanoshell. For the superradiant mode on the long wavelength side, the largest fields are induced between the central nanoshell and its directly adjacent particles. At the dip, both modes are excited.

To examine the role of phase retardation in these coupled plasmonic systems in greater detail, we performed FDTD calculations of the optical spectra of the four structures whose spectra are displayed in Figure 4, scaling down all dimensions by a common factor ranging from a 1.1 to 8, thus continuously reducing the effects of retardation. In the electrostatic limit, such a scale transformation would leave the optical spectra invariant.

In Figure 5a we show the FDTD extinction spectra for a single nanoshell, trimer, septamer, and array for a scaling factor of 8, setting the overall dimensions of the nanoshells to 21.5 nm and their separation to 1 nm. Below, in Figure 5b, the spectra of the same structures cal-

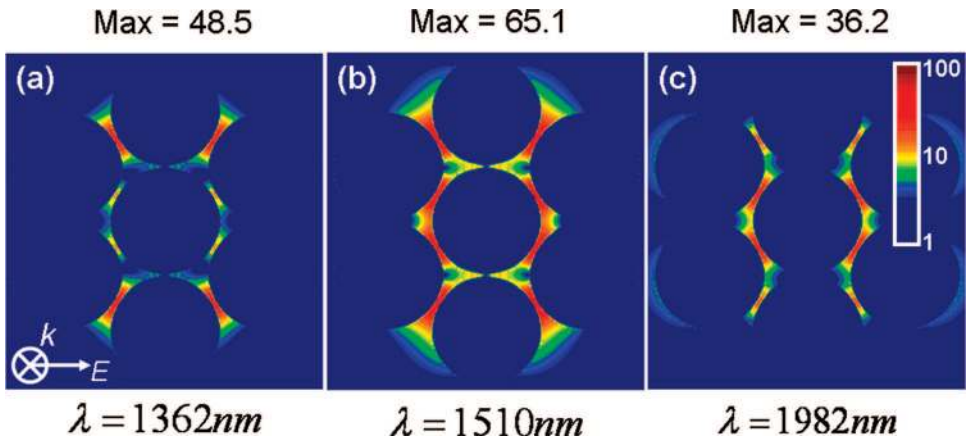

Figure 4. Local electromagnetic field enhancements for the nanoshell septamer in Figure 3 at wavelengths of 1362, 1510, and 1982 nm, calculated using the FDTD method.

culated using the electrostatic plasmon hybridization (PH) method are shown.[46,47] The quadrupolar resonances can clearly be seen in the spectra of the trimer, septamer, and the array, as a shoulder and peak just below 1000 nm. The dipolar resonances of the individual nanoshell, nanoshell trimer, nanoshell septamer, and the HCP nanoshell array appear at 1000, 1330, 1300, and 2070 nm, respectively. The energies of these modes are blue-shifted compared to the larger structures in Figure 4 due to weaker retardation. Since retardation effects always cause a redshift of dipolar resonances, Figure 5a suggests that the location of the strongly damped dipolar resonance in the real HCP nanoshell array should be positioned at a wavelength significantly larger than 2070 nm.

Plasmon Hybridization Analysis. A comparison of the FDTD for the scaled-down structures and the PH spectra in Figure 5 shows very good agreement, with the corresponding plasmon modes showing up at very similar wavelengths. Since the optical absorption in the PH method is proportional to the square of the dipole moment of the plasmon mode while the FDTD calculation also includes coupling to higher multipoles, the relative peak intensities in PH and FDTD spectra can be different. For this reason, the quadrupolar modes do not show up in the PH spectra of the individual nanoshell but are clearly visible in the larger structures because of the hybridization of quadrupolar and dipolar plasmon on adjacent nanoparticles. The slight blueshift of the PH spectra compared to the FDTD spectra is due to the complete neglect of phase retardation in the PH method. The most noticeable difference between the PH and FDTD spectra is the width of the array resonance. In the PH method, the width of the resonance originates entirely from the imaginary part of the dielectric function. In the FDTD calculation, radiative damping also contributes to the line width.

It is quite interesting and significant that an electrostatic approach such as the PH method can reproduce the peak positions of an infinite periodic system. This is because the interactions between plasmons on different nanoparticles decrease rapidly with nanoparticle separation. The plasmon energies are thus determined by the local structure of the array. This local region includes nearest and next nearest neighbors. Therefore, if the size of the local region is much smaller than the wavelength of incident light, the energies of the plas-

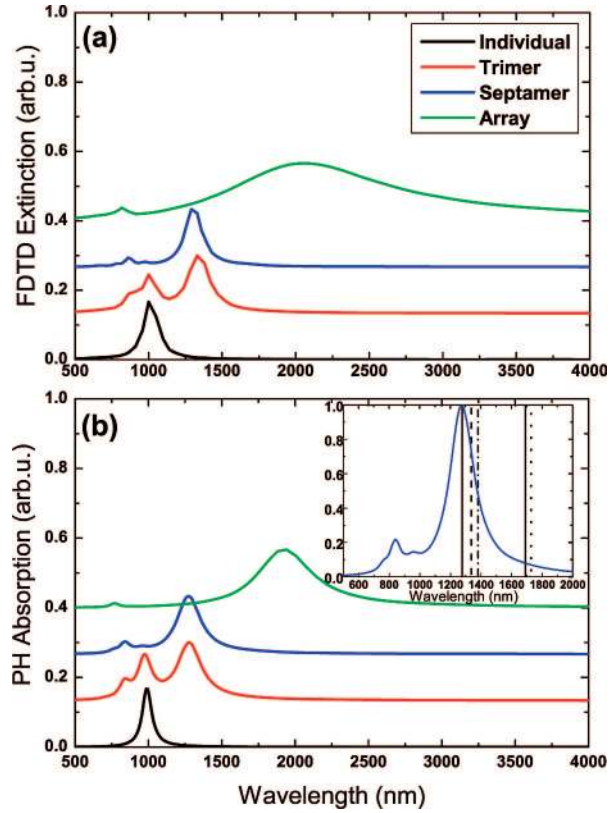

Figure 5. FDTD extinction spectra (a) and PH absorption spectra (b) of an individual nanoshell (black), a nanoshell trimer (red), a nanoshell septamer (blue), and an HCP nanoshell array (green). The inset in panel b shows the energy and symmetry of the five lowest energy plasmon modes: E_{1u} (solid), A_{2g} (dotted), E_{2g} (dot-dashed), and B_{1u} (dashed) for the septamer calculated using PH. The size of nanoshells in each case is $(r_1, r_2) = (18.75,21.5)$ nm, and the separation is $d = 1$ nm. The calculations were performed using a pure Drude dielectric function with $\omega_B = 4.6$ eV and a damping of 0.15 eV.

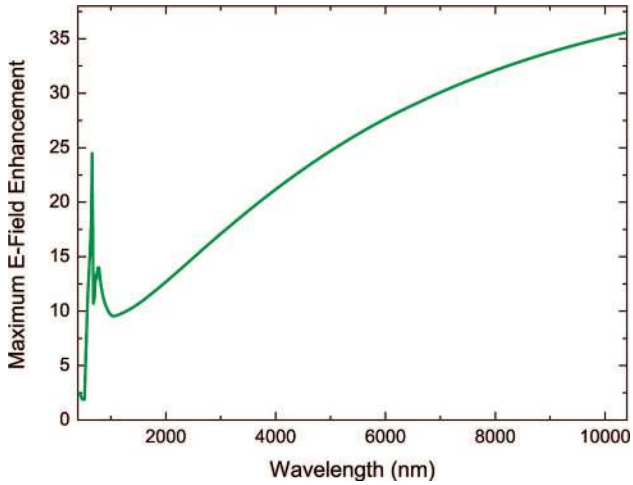

Figure 6. Maximum electric field enhancement in the junctions of a HCP nanoshell array as a function of wavelength. The simulations are performed using COMSOL Multiphysics 3.3a. At MIR to IR regime (wavelength >2000 nm) the maximum field enhancement steadily increases towards 35 at 10 μm. The maximum electric field enhancement saturates to a value around 40 beyond 20 μm.

mon modes can be described using an electrostatic approach.

Group Theoretical Analysis. The spectrum of the small septamer in Figure 5a does not display a Fano resonance. A careful analysis of the septamer spectra for different scaling factors shows that the superradiant mode redshifts much more strongly than the subradiant mode with decreasing scaling factor. For scaling factors smaller than 2, the energies of the two modes are similar and the subradiant mode appears as an asymmetric dip in the spectrum. For smaller systems (scaling factors larger than 2), the energy of the subradiant mode is lower than that of the superradiant mode, and the subradiant mode appears as a positive peak on the red side of the superradiant peak. The PH method provides a simple group theoretical analysis of the microscopic nature of the plasmon modes in a multiparticle aggregate based on their symmetry.[46,48] The point group of the septamer is D_{6h}. In the inset of Figure 5b, we show the energies and irreducible representations of the five lowest energy plasmon modes of the septamer. The sub- and superradiant modes are the two modes belonging to the E_{1u} irreducible representation. In the superradiant mode the nanoshell in the center of the septamer has in-phase plasmonic oscillations with the six other peripheral nanoshells, inducing a strong radiative damping and a broad peak in the spectrum. In the subradiant mode, the plasmons in the central nanoshell oscillate out-of-phase with the plasmons of the peripheral nanoshells, so that the radiative damping is strongly suppressed. The higher energy superradiant mode has a large dipole moment while the subradiant mode has no net dipole moment. The subradiant mode can therefore only be excited through its quadrupolar resonant modes.

Analysis of the Experimental Array Spectrum. We can now explain in more detail the difference between the experimental spectra in Figure 1 and the FDTD spectra in Figure 2. The FDTD calculation, with its assumption of a perfectly periodic array, overestimates the radiative damping actually observed in the experimental sample. The defects in the experimentally fabricated nanoshell arrays discussed earlier can localize the plasmon modes and introduce inhomogeneous broadening. Any deviation from perfect periodicity will also break the coherence of the collective dipolar plasmon mode and can lead to destruction of the superradiance.[49] For dipoles oscillating out of phase, the radiative damping can become smaller than the radiative damping of an individual dipole which leads to subradiance.[50] From the perspective of coherence, in the presence of a small degree of disorder, the substrate can probably best be described as consisting of independent, finite-sized domains within which coherence is maintained. These optical coherence effects only influence the damping of the plasmon resonance and not their energies, which are determined by local properties, that is, the hybridization of individual nanoparticle plasmons with adjacent nanoparticles. The fact that the calculated trimer and septamer spectra in Figure 3 look much more similar to the experimental spectrum of Figure 1 than the calculated array spectra supports this hypothesis. However, even the septamer dipolar resonance is considerably narrower than the experimental MIR resonance, indicating that the size of the coherent domains are likely to be larger than a nanoparticle septamer.

Electric Field Enhancements. In Figure 2 we showed that significant electric field enhancements were induced at the same locations (in the junctions) of the HCP nanoshell array for two very different wavelengths, a NIR resonance of relevance for SERS and a MIR resonance of relevance for SEIRA. As discussed in the introduction, this is a finding of considerable importance in sensing applications since it allows the use of two complementary vibrational spectroscopies for the detection of the same analyte at the same spot on the same substrate. In this section we will further analyze the physical mechanisms underlying these enhancements.

In Figure 6 we show the calculated maximum electric field enhancements in the 2D HCP nanoshell array as a function of the wavelength of the incident light. Further investigation shows that the maximum field enhancement factor continues to grow until it saturates at a value of around 40 beyond 20 μm. The peak in the field enhancement around 750 nm is due to the resonant excitation of the NIR quadrupolar plasmon. This mode is only weakly damped, which allows for an efficient pumping of the quadrupolar oscillator. The electromagnetic field enhancements associated with this mode therefore have a wavelength dependence similar to that of the far field extinction spectrum. In con-

trast, the large field enhancements for the largest wavelengths can be understood as an electrostatic lightning-rod effect.[51,52] The slow monotonic increase of the maximum field enhancement between the wavelengths of 2 and 20 μm can be understood simply as the response of an overdamped dipolar harmonic oscillator. Only for very slow perturbations will the oscillator adjust adiabatically to the applied force. The screening associated with the lightning-rod effect does not correspond to excitations of plasmons and will therefore not appear in the far-field excitation spectrum.

The calculated field enhancement of approximately 35 in the MIR corresponds to electromagnetic SEIRA enhancement factors of 10^3 (35^2). These values are consistent, but slightly lower than, the largest SEIRA enhancement factors of 6×10^4 reported in the experimental SEIRA study of pMA.[37] Possible reasons for this discrepancy may be structural inhomogeneities in the array (closer separations between two adjacent nanoshells), or chemical effects, that is, an increase in the dynamical dipole moment of some of the vibrational modes of a molecule chemisorbed on a nanoparticle surface.

Lightning-Rod Effect. The relevance of the lightning-rod effect for the understanding of the large field enhancements in nanoparticle dimers was recently discussed by Käll and co-workers.[53] The physical origin of the lightning-rod effect is metallic screening. For a perfect metal, no electric field penetrates inside the material. The metal becomes equipotential and all potential drops must occur in the junctions between the metals. Indeed, the electric field enhancement plot in Figure 2c shows this effect already at 3 μm, with the electric field almost perfectly expelled from the metallic shells. The reason for the efficient screening of metals at low frequencies is that the real part of the dielectric function becomes large and negative. The expulsion of the electric field from the interior of the nanoparticles gives rise to the intense field enhancements in the junctions between the metals. This phenomenon provides yet another simple way of understanding the slow monotonic increase of the maximum field enhancement in Figure 6. As the wavelength is increased and the dielectric permittivity becomes more and more negative, the electric field are gradually expelled from the metallic shells with a resulting increase in the field strength in the junctions.

Our finding of large electric field enhancements in metallic structures at long wavelengths in nanoparticle arrays is not limited to nanoshells. Our results would apply equally well to finite aggregates of arbitrarily shaped nanoparticles as long as the wavelength of incident light is in the mid- to far-infrared, thus, resulting in an extremely versatile system to perform highly efficient SEIRA spectroscopy independently of the structural constitution of the array unit cell.

In the original work on the relevance of the lightning-rod effect for SERS on individual nanoparticles, it was noted that the structure of the particles will influence both the magnitude of the maximum field enhancement and the volume within which the field enhancements remain large.[52] To investigate if this applies to arrays, we now use a simple electrostatic approach and investigate the field enhancements in two-dimensional square lattices of metallic spheres, cylinders, and blocks. The simulations were performed using the electrostatic module of COMSOL Multiphysics 3.3a,[54] which is a finite-element-based commercial numerical simulation software.

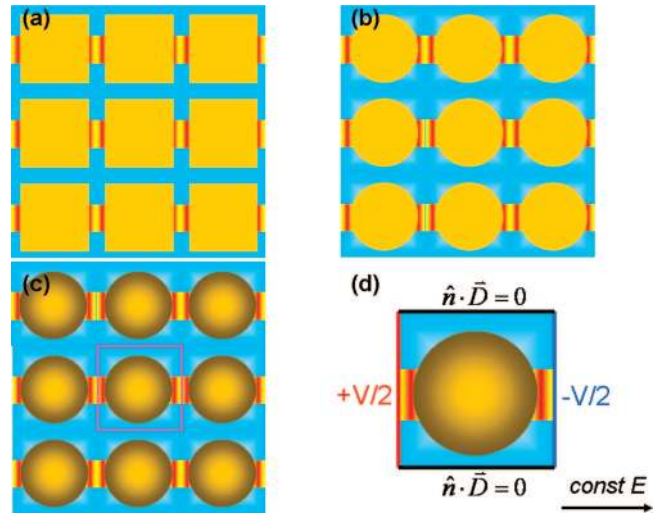

Figure 7. Schematic illustration of a typical COMSOL simulation on a 2D square lattice of (a) blocks, (b) cylinders, and (c) spherical particles. The particles are perfect conductors with a diameter *D* and interparticle separation *d* . Panel d shows the individual unit cell of the lattice. The left and right boundaries are equipotential boundaries with electric potentials *V*/2 and −*V*/2, respectively. The location of the hotspots in the nanoparticle junctions are illustrated in red and yellow.

In Figure 7 we schematically illustrate the numerical experiment. The structures are periodic square lattices as illustrated in panel a. For the cylinders and blocks when the separation distance *d* is small compared to the overall size of the individual structures *D*, the maximum field enhancement E_{max} occurs in the middle of the junction between two adjacent particles. For the spheres, a slightly larger field enhancement (10%) can sometimes be found on the sphere surface. For consistency, we will define the maximum field enhancement as the value in the middle of the junction. Using PBC the calculation of the fields needs only to be performed in a unit cell as shown in panel d. The left and right boundaries are set to be equipotential surfaces with electric potentials *V*/2 and −*V*/2, respectively. For the other boundaries we apply symmetric (zero charge) boundary conditions. When the separation *d* is changed, *V* is tuned so that the background electric field across the unit cell without any objects $E_0 = V/(D + d)$ is a constant, where D is the dimension of the object. For simplicity the dielectric constant of the objects is set to minus infinity, as appropriate for a perfect con-

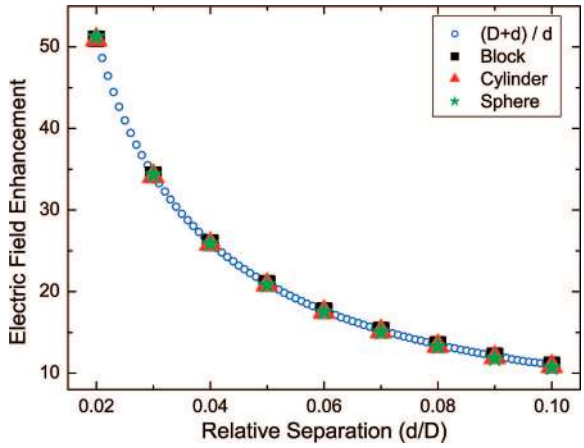

Figure 8. The maximum electric field enhancement factor η as a function of relative separation *d*/*D* for sphere, cylinder, and block arrays, respectively. The relation between η and *d*/*D* in these three systems almost overlap and can be parametrized as $\eta = (D + d)/d$.

ductor. The maximum field enhancement η is defined as $\eta = E_{max}/E_0$.

Maximum Field Enhancement. In Figure 8, the calculated maximum electric field enhancement factor for the sphere, cylinder, and block arrays as a function of relative separation *d*/*D* for thin junctions is shown. We also show the analytical result $\eta = (D + d)/d$ for the field enhancement in a junction of thickness *d* between two metallic spheres of diameter *D* derived previously using electrostatic arguments.[53] In this approach, the enhancement factor $\eta = E_{loc}/E_i$ which is the ratio of the incident field E_i and the local field E_{loc}, can be derived from the condition for the potential $E_i(D + d) = E_{loc}d$, obtaining $E_{loc}/E_i = (D + d)/d$.[53] The results show almost identical field enhancement factors. The fact that the relation between η and *d*/*D* is the same for these very different structures is a consequence of perfect metallic screening. The maximum field enhancement is only dependent on the closest distance between two equipotential particles and not on the detailed structure around the junction.

In Figure 9 we show the calculated local electric fields and the electrostatic equipotential surfaces of the cylinder and the block arrays. For the cylinder array there is a distinct hotspot (Figure 9b) but for the block array (Figure 9e) the electric field is almost uniformly distributed in the junctions. Although the spatial distributions of the field enhancement are quite different, the maximum field enhancement factors are the same for both systems. In panels c and f we show the electrostatic equipotential surfaces of these two systems. Although the overall electric potential distributions are different for the block and the cylinder array, the close-up around the hot-spots are nearly identical.

In this analysis we have studied arrays of nanoparticles with the same aspect ratio in their lateral dimensions. The magnitude of the maximum field enhancements in the electrostatic limit will depend on the aspect ratio of the individual particles.

Hotspot Volume. A factor of crucial importance for the efficiency of a substrate for SES is associated with the

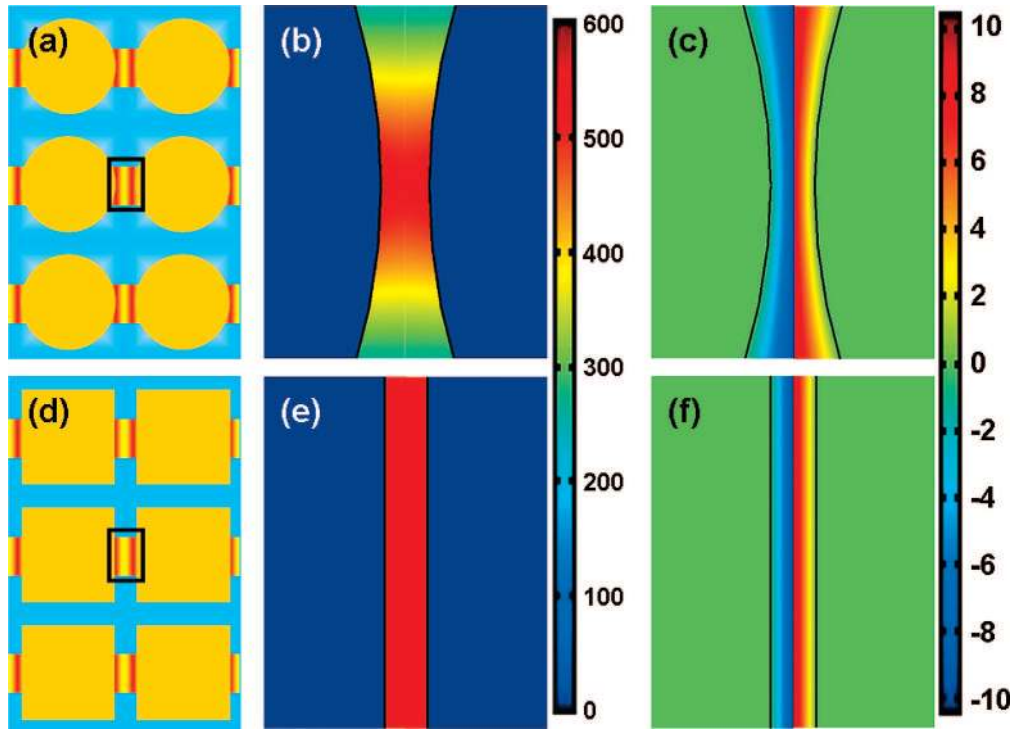

Figure 9. Local electric field enhancements and electrostatic potential surfaces for the 2D cylinder and block arrays. The applied electric field is $E_0 = 20$ and the relative separation is $d/D = 0.04$. Panels a,d show the cylinder and block array schematically with inset; Panels b,e show the electric field enhancements for the cylinder and the block array insets; Panels c,f display the electric potential distribution in the cylinder array and the block array insets, respectively.

sensing volume, that is, the volume inside which the electromagnetic field enhancements are large. A large hotspot volume means that a larger number of molecules can be probed. We now investigate how the hotspot volume of conductive arrays (an assumption valid to describe behavior in the infrared as a SEIRA substrate) depends on interparticle separation and shape of the particles. Since the electric field enhancements can vary significantly in space and their relevance for different SES depends on how the cross sections depend on the power of the field enhancement, the hotspot volume needs to be defined differently for different spectroscopies. For SEIRA we define the SEIRA efficiency as

$$\Sigma = \int E^2 dV, \quad (1)$$

with a hotspot volume defined as $V_H = \Sigma/E_{max}^2$. To evaluate the integral we need to do a subdomain integration of energy density $E^2 dV$ for each system.

In Figure 10, the calculated hotspot volume for the sphere, cylinder, and block arrays as a function of particle separation is shown. On a logarithmic scale, the calculated V_H of these three arrays each follows an almost perfect linear dependence on d/D and can be parametrized as

$$V_H^B \propto (d/D)^{1.035} \quad (2)$$

$$V_H^C \propto (d/D)^{1.431} \quad (3)$$

$$V_H^S \propto (d/D)^{1.742} \quad (4)$$

These results can simply be rationalized by analyzing the surface curvatures of the different particles. For the blocks, the surfaces are flat so that the lateral size of the hotspot always equals the surface area of the particles. Hence V_H increases linearly with separation. For the cylindrical particles, the lateral size of hotspot in the plane parallel to the cylinder axis is constant, while the dimension in the plane perpendicular to the cylinder axis is proportional to $(d/D)^{0.5}$. Thus V_H of the cylindrical particles should be proportional to $(d/D)^{1.5}$. For the spherical particles the lateral dimension of the hotspot should be proportional to $(d/D)^{0.5}$ which would lead to V_H being proportional to $(d/D)^2$. We believe that the reason the simple geometrical analysis does not work exactly for the sphere array is caused by the more inhomogeneous field distribution in the sphere array relative to the cylinder and block arrays. An explicit calculation of the volume within which the field enhancement remains larger than 10% of the maximum enhancement gives the powers 1.038, 1.494, and 2.033 for the block, cylinder, and sphere arrays, respectively. The hotspot volumes for the block arrays are much larger and homogeneous than for the sphere arrays, with those for the cylinder array in between. Since the maximum field enhancements depend only on interparticle separation, the block or cylinder arrays provide better SEIRA substrates than 2D sphere arrays.

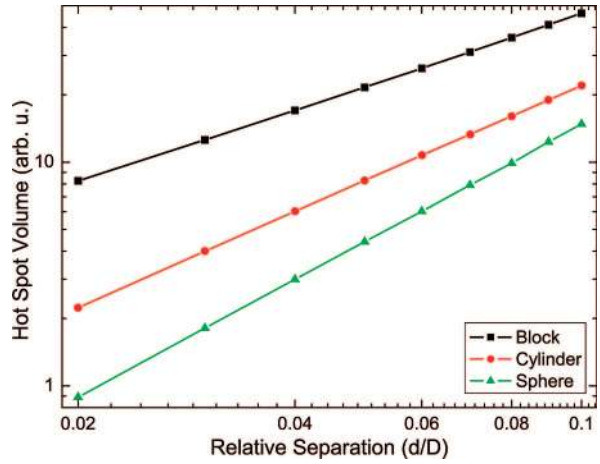

Figure 10. Hotspot volume V_H as a function of separation d/D for 2D square arrays of block, cylinder, and sphere particles. The figure is plotted on a log–log scale and the slopes are 1.035 (B), 1.431 (C), and 1.742 (S).

Designing an Efficient SEIRA Substrate. We now demonstrate how our findings can be applied to optimize a configuration of metallic nanoparticles on a finite-sized substrate for maximum SEIRA efficiency. For simplicity, we consider a single layer square array of rectangular metallic blocks of length L, width W, and height W, separated by junctions of a length d. What is the optimal shape of the individual particles for a given substrate area? For simplicity we will assume light incident perpendicular to the substrate. Our electrostatic analysis shows that the maximum field enhancements in the junctions for longitudinal polarization (polarization along L) is proportional to $(L + d)/d$. The corresponding hotspot volume will be proportional to $W^2 d$ with a SEIRA efficiency proportional to $(L + d)^2 W^2/d$. For transverse polarization (polarization along W), the maximum field enhancement is $(W + d)/d$ with a hotspot volume of LWd. The SEIRA efficiency for transverse polarization is thus $(W + d)^2 LW/d$. The surface footprint per particle is $(L + d)(W + d)$. By maximizing the SEIRA efficiency for a fixed particle foot print area, it can trivially be shown that the optimal SEIRA efficiency per unit surface area is achieved for longitudinal polarization and high aspect ratio (L/W) particles. Such a substrate may be realized by aligning finite carbon nanotubes on the substrate,[55] or by electron or focused ion beam milling of a thin metallic film. For more complicated structures, the optimization problem becomes a multivariable problem which can straightforwardly be solved using linear programming methods such as the Simplex Method.[56]

CONCLUSIONS

Using the FDTD, PH, and FEM methods we have analyzed the electromagnetic properties of two-

dimensional hexagonal nanoshell arrays. We have shown that the extinction spectrum for normal incidence is characterized by a narrow resonance in the NIR and a broad structure in the MIR in qualitative agreement with experimental results. These resonances are formed through interactions and hybridization of the individual nanoshell plasmons. The NIR resonance originates from the quadrupolar resonances of the individual nanoshells and the MIR resonance derives from the dipolar resonances of the individual nanoshells. The strong broadening of the MIR resonance is caused by radiative damping which for normal incidence results in superradiance, that is, a collective enhancement of the radiation from several dipolar emitters oscillating in phase. An analysis of the electromagnetic field enhancements in the array structure reveals large field enhancements in the nanoparticle junctions both for the excitation of the NIR and the MIR modes. The field enhancements associated with the NIR resonance can be understood as a conventional resonant excitation of a weakly damped plasmon mode, with a wavelength dependence that follows the extinction spectrum. The field enhancements associated with the MIR resonance show a qualitatively different wavelength dependence with a slow monotonic increase with increasing wavelength and a saturation to the electrostatic result at a wavelength beyond 20 μm. The field enhancements induced in the MIR are not caused by excitations of plasmons but are a consequence of metallic screening, that is, the lightning-rod effect. At long wavelengths, metals behave like perfect equipotential conductors and all the field enhancements result from the drop of the potentials across the junctions between individual nanoparticles. In this limit, the field enhancements depend only on the geometrical structure of the substrate. The slow increase of the field enhancements in the MIR is analogous to the response of an overdamped oscillator and is consistent with our finding of large radiative damping of the MIR resonance. Our observation that the maximum field enhancement in the MIR does not depend sensitively on wavelength is another advantage for SEIRA where the measurements need to be performed over an extended spectral region.

We have demonstrated that the field enhancement and hotspot volumes in the infrared region of the spectrum where SEIRA takes place can be described using analytical electrostatic arguments. Following this simple but practical approach, we have identified the structural requirements for optimization of a substrate for maximum SEIRA efficiency in a very general way. Our initial investigations indicate that such a substrate should be composed of high aspect ratio particles. In contrast to the hotspots associated with resonant excitation of plasmons in SERS, high field enhancements in the far-infrared do not require sharp junctions, but rather the use of narrow flat junctions with large hotspot volumes. The field enhancement is also more constant and homogeneous compared to the plasmon resonances in the visible and near IR, therefore the common magnification of the infrared signal has the advantage of preserving the information on the relative weight of the absorption peaks. Moreover, because the nature of the enhancement in the far-infrared is connected with the exclusion of the field from the conductor-like material, the trends for optimizing the enhancement can be extrapolated to Terahertz frequency regions, thus having a great potential for SEIRA in this relatively unexplored spectral range. The concepts shown in this communication could lead to a new paradigm in the design of efficient substrates for visible (SERS) and far-infrared (SEIRA) spectroscopies.

METHODS

Experiments. Au nanoshells were fabricated following a previously reported seed-mediated electroless plating method,[24] then purified by dialysis. The dialyzed nanoshells were functionalized with the surfactant cetyltrimethyl ammonium bromide (CTAB), and subsequently redispersed in water to form colloidal solutions with desired particle concentrations. Applying droplets of nanoshell solution to a substrate and allowing the solvent to evaporate under ambient conditions resulted in the formation of hexagonally packed nanoshell arrays, which maintain an interparticle spacing established by the bilayers of CTAB that surround each nanoshell as the interparticle spacer. The nanoshells organize into hcp structures with typical domain sizes ranging from several tens of micrometers to over two hundred micrometers. The CTAB molecules form bilayer structures on the surface of Au nanoparticles, resulting in a net positive charge on the nanoparticle surfaces, and providing a net repulsive interaction between the nanoparticles to prevent random disordered aggregation during solvent evaporation. The CTAB bilayers also define the spacing between neighboring nanoshells and result in an average interparticle spacing determined to be nominally 8 nm, consistent with the reported thickness of a CTAB bilayer. Optical spectroscopic measurements were performed on nanoshell monolayer arrays formed on glass slides using unpolarized light at normal incidence with a commercial UV–vis spectrophotometer.

Finite-Difference Time-Domain Method. The FDTD method is an established numerical time marching algorithm for the solution of Maxwell's equations on a spatial grid.[57] The method provides an accurate and fully retarded description of both the near- and far-field properties of the electromagnetic response. Our implementation has been parallelized for execution on distributed memory computer architectures such as Beowulf clusters using domain decomposition.[39,58]

Plasmon Hybridization Method. The PH method is an electrostatic method for calculating the energies of plasmon resonances and the optical absorption spectra of complex nanostructures. The method has recently been reviewed with references to many applications,[30] briefly, the plasmons of a composite metallic nanostructure are expressed as a linear combination of the plasmons in the individual parts or surfaces of the nanostructure. The kinetic and electrostatic energy of the system is calculated using a Lagrangian approach. By application of the Euler–Lagrange equation, the plasmon energies are obtained from a secular equation. The structure of the eigenvalue problem is then equivalent to the secular equation in molecular orbital theory describing how electronic levels interact (hybridize) and

shift in the presence of interactions. The plasmon hybridization method provides a simple and intuitive method for understanding the nature of the plasmon resonances in composite nanostructures.

Finite Element Method. The FEM method is standard method for the solution of partial differential equations. Briefly, the electromagnetic field are expanded in finite elements, that is, basis functions localized around individual points on a spatial grid. Using a variational formulation, Maxwell's equations are converted to matrix equations which are solved using direct or iterative methods. Our FEM calculations are performed using the electrostatic module of COMSOL Multiphysics 3.3a,[54] which is a finite-element-based commercial numerical simulation software.

Acknowledgment. This work is supported by the U.S. Army Research Laboratory and the U.S. Army Research Office under contract/grant no. W911NF-04-1-0203, the Robert A. Welch Foundation under grants C-1220 and C-1222, by NSF under grants EEC-0304097, CNS-0421109, ECCS-0421108, and DMR-0705384, and by the Air Force Office of Scientific Research Grant FA9550-06-1-0021. J.A. acknowledges the friendly and hospitable atmosphere at the Rice Laboratory for Nanophotonics during a one months stay in the summer and financial support from the ETORTEK NANOTRON project.

REFERENCES AND NOTES

1. Xu, H.; Aizpurua, J.; Kall, M.; Apell, P. Electromagnetic Contributions to Single-Molecule Sensitivity in Surface-Enhanced Raman Scattering. *Phys. Rev. E* **2000**, *62*, 4318–4324.
2. Li, K.; Stockman, M. I.; Bergman, D. J. Self-Similar Chain of Metal Nanospheres as an Efficient Nanolens. *Phys. Rev. Lett.* **2003**, 91.
3. Moskovits, M.; Jeong, D. H. Engineering Nanostructures for Giant Optical Fields. *Chem. Phys. Lett.* **2004**, *397*, 91–95.
4. Maier, S. A.; Atwater, H. A. Plasmonics: Localization and Guiding of Electromagnetic Energy in Metal/Dielectric Structures. *J. Appl. Phys.* **2005**, *98*, 011101.
5. Urzhumov, Y. A.; Shvets, G. Applications of Nanoparticle Arrays to Coherent Anti-Stokes Raman Spectroscopy of Chiral Molecules. *Proc. SPIE* **2005**, *5927*, 59271D.
6. Qin, L.; Zou, S.; Xue, C.; Atkinson, A.; Schatz, G. C.; Mirkin, C. A. Designing, Fabricating, and Imaging Raman Hot Spots. *Proc. Natl. Acad. Sci. U.S.A.* **2006**, *103*, 13300–13303.
7. Zhu, J. Spatial Dependence of the Local Field Enhancement in Dielectric Shell Coated Silver Nanoparticles. *Appl. Surf. Sci.* **2007**, *253*, 8729–8733.
8. Evans, P. R.; Wurtz, G. A.; Atkinson, R.; Hendren, W.; O'Connor, D.; Dickinson, W.; Pollard, R. J.; Zayats, A. V. Plasmonic Core/Shell Nanorod Arrays: Subattoliter Controlled Geometry and Tunable Optical Properties. *J. Phys. Chem. C* **2007**, *111*, 12522–12527.
9. Zhang, J.; Chowdhury, M. H.; Lakowicz, J. R. Metal-Enhanced Single-Molecule Fluorescence on Silver Particle Monomer and Dimer: Coupling Effect between Metal Particles. *Nano Lett.* **2007**, *7*, 2101–2107.
10. Dmitriev, A.; Pakizeh, T.; Kall, M.; Sutherland, D. S. Gold-Silica-Gold Nanosandwiches: Tunable Bimodal Plasmonic Resonators. *Small* **2007**, *3*, 294–299.
11. Johansson, P.; Xu, H. X.; Kall, M. Surface-Enhanced Raman Scattering and Fluorescence Near Metal Nanoparticles. *Phys. Rev. B* **2005**, *72*, 035427.
12. Gibson, J. W.; Johnson, B. R. Density-Matrix Calculations of Surface Enhanced Raman Scattering for *p*-Mercaptoaniline on Silver Nanoshells. *J. Chem. Phys.* **2006**, *124*, 064701.
13. Janesko, B. G.; Scuseria, G. E. Surface Enhanced Raman Optical Activity of Molecules on Orientationally Averaged Substrates: Theory of Electromagnetic Effects. *J. Chem. Phys.* **2006**, *2006*, 124704.
14. Goude, Z. E.; Leung, P. T. Surface Enhanced Raman Scattering from Metallic Nanoshells with Nonlocal Dielectric Response. *Solid State Commun.* **2007**, *143*, 416–420.
15. Osawa, M. Surface-Enhanced Infrared Absorption. *Top. Appl. Phys.* **2001**, *81*, 163–187.
16. Jensen, T. R.; van Duyne, R. P. Surface-Enhanced Infrared Spectroscopy: A Comparison of Metal Island Films with Discrete and Nondiscrete Surface Plasmons. *Appl. Spectrosc.* **2000**, *54*, 371–377.
17. Goutev, N.; Futamata, M. Attenuated Total Reflection Surface-Enhanced Infrared Absorption Spectroscopy of Carboxyl Terminated Self-Assembled Monolayers of Gold. *Appl. Spectrosc.* **2003**, *57*, 506–513.
18. Carrasco, E. A.; Vallette, F. M. C.; Leyton, P.; Diaz, G.; Clavijo, R. E.; Garcia-Ramos, J. V.; Inostroza, N.; Domingo, C.; Sanchez-Cortez, S.; Koch, R. Study of Interaction of Pollutant Nitro Polycyclic Aromatic Hydrocarbons with Different Metallic Surfaces by Surface-Enhanced Vibrational Spectroscopy (SERS and SEIRA). *J. Phys. Chem. A* **2003**, *107*, 9611–9619.
19. Ataka, K.; Giess, F.; Knoll, W.; Naumann, R.; Haber-Pohlmeier, S.; Richter, B.; Heberle, J. Oriented Attachment and Membrane Reconstitution of HIS-Tagged Cytochrome C Oxidase to a Gold Electrode: In Situ Monitoring by Surface-Enhanced Infrared Absorption Spectroscopy. *J. Am. Chem. Soc.* **2004**, *49*, 16199–16206.
20. Rodriguez, K.; Shah, S.; Williams, S. M.; Teters-Kennedy, S.; Coe, J. V. Enhanced Infrared Absorption Spectra of Self-Assembled Alkanethiol Monolayers using the Extraordinary Infrared Transmission of Metallic Arrays of Subwavelength Apertures. *J. Chem. Phys.* **2004**, *121*, 8671–8675.
21. Enders, D.; Rupp, S.; Kuller, A.; Pucci, A. Surface Enhanced Infrared Absorption on Au Nanoparticle Films Deposited on SiO_2/Si for Optical Biosensing: Detection of the Antibody-Antigen Reaction. *Surf. Sci.* **2006**, *600*, L305–L308.
22. Ataka, K.; Heberle, J. Biochemical Applications of Surface-Enhanced Infrared Absorption Spectroscopy. *Analyutical and Bioanalytical Chemistry* **2007**, *388*, 47–54.
23. Kundu, J.; Le, F.; Nordlander, P.; Halas, N. J. Surface Enhanced Infrared Absorption (SEIRA) Spectroscopy on Nanoshell Aggregate Substrates. *Chem. Phys. Lett.* **2008**, *452*, 115–119.
24. Oldenburg, S.; Averitt, R. D.; Westcott, S.; Halas, N. J. Nanoengineering of Optical Resonances. *Chem. Phys. Lett.* **1998**, *288*, 243–247.
25. Link, S.; El-Sayed, M. A. Spectral Properties and Relaxation Dynamics of Surface Plasmon Electronic Oscillations in Gold and Silver Nanodots and Nanorods. *J. Phys. Chem. B* **1999**, *103*, 8410–8426.
26. Jensen, T. R.; Malinsky, M. D.; Haynes, C. L.; van Duyne, R. P. Nanosphere Litography: Tunable Localized Surface Plasmon Resonance Spectra of Silver Nanoparticles. *J. Phys. Chem. B* **2000**, *104*, 10549–10556.
27. Kelly, K. L.; Coronado, E.; Zhao, L. L.; Schatz, G. C. The Optical Properties of Metal Nanoparticles: The influence of Size, Shape, and Dielectric Environment. *J. Phys. Chem. B* **2003**, *107*, 668–677.
28. Aizpurua, J.; Hanarp, P.; Sutherland, D. S.; Kall, M.; Bryant, G. W.; de Abajo, F. J. G. Optical Properties of Gold Nanorings. *Phys. Rev. Lett.* **2003**, *90*, 057401.
29. Neubrech, F.; Kolb, T.; Lovrincic, R.; Hahsold, G.; Pucci, A.; Aizpurua, J.; Cornelius, T. W.; Toimil-Molares, M. E.; Neuman, R.; Karim, S. Resonances of Individual Metal Nanowires in the Infrared. *Appl. Phys. Lett.* **2006**, *89*, 253104.
30. Wang, H.; Brandl, D. W.; Nordlander, P.; Halas, N. J. Plasmonic Nanostructures: Artificial Molecules. *Acc. Chem. Res.* **2007**, *40*, 53–62.
31. Liu, N.; Guo, H.; Fu, L.; Kaiser, S.; Schweizer, H.; Giessen, H. Plasmon Hybridization in Stacked Cut-Wire Metamaterials. *Adv. Mater.* **2007**, *19*, 3628–3632.
32. Bukasov, R.; Shumaker-Parry, J. S. Highly Tunable Infrared Extinction Properties of Gold Nanocrescents. *Nano Lett.* **2007**, *7*, 1113–1118.
33. Jain, P. K.; El-Sayed, M. A. Universal Scaling of Plasmon Coupling in Metal Nanostructures: Extension from

Nanoparticle Pairs to Nanoshells. *Nano Lett.* **2007**, *7*, 2854–2858.
34. Khlebtsov, B. N.; Khanadeyev, V. A.; Ye, J.; Mackowski, D. W.; Borghs, G.; Khlebtsov, N. G. Coupled Plasmons Resonances in Monolayers of Metal Nanoparticles and Nanoshells. *Phys. Rev. B* **2008**, *77*, 035440.
35. Tserkezis, C.; Gantzounis, G.; Stefanou, N. Collective Plasmonic Modes in Ordered Assemblies of Metallic Nanoshells. *J. Phys.: Condens. Matter* **2008**, *20*, 075232.
36. Jackson, J. B.; Halas, N. J. Surface Enhanced Raman Scattering on Tunable Plasmonic Nanoparticle Substrates. *Proc. Nat. Acad. Sci. U.S.A.* **2004**, *101*, 17930–17935.
37. Wang, H.; Kundu, J.; Halas, N. J. Plasmonic Nanoshell Arrays Combine Surface-Enhanced Vibrational Spectroscopies on a Single Substrate. *Angew. Chem., Int. Ed.* **2007**, *46*, 9040–9044.
38. Taflove, A. *Advances in Computational Electrodynamics: The Finite-Difference Time Domain Method*; Artech House, Inc.: Norwood, MA, 1998.
39. Oubre, C.; Nordlander, P. Optical Properties of Metallodielectric Nanostructures Calculated using the Finite Difference Time Domain Method. *J. Phys. Chem. B* **2004**, *108*, 17740–17747.
40. Dicke, R. H. The Effect of Collisions upon the Doppler Width of Spectral Lines. *Phys. Rev.* **1953**, *89*, 472–473.
41. Bar-Gill, N.; Rowen, E. E.; Davidson, N. Spectroscopy of Strong-Pulse Superradiance in a Bose-Einstein Condensate. *Phys. Rev. A* **2007**, *76*, 043603.
42. Mogyorosi, K.; Kelley, D. F. Superradiance in GaSe Nanoparticle Aggregates. *J. Phys. Chem. C* **2007**, *111*, 579–585.
43. Creek, S.; Efthimiou, O.; Kanti, P.; Tamrakis, K. Scalar Emission in the Bulk in a Rotating Black Hole Background. *Phys. Lett. B* **2007**, *656*, 102–111.
44. Ropers, C.; Park, D. J.; Steinmeyer, G.; Kim, D. S.; Lienau, C. Femtosecond Light Transmission and Subradiant Damping in Plasmonic Crystals. *Phys. Rev. Lett.* **2005**, *94*, 113901.
45. Christ, A.; Ekinci, Y.; Solak, H. H.; Gippius, N. A.; Tikhodeev, S. G.; Martin, O. J. F. Controlling the Fano Interference in a Plasmonic Lattice. *Phys. Rev. B* **2007**, *76*, 201405R.
46. Brandl, D. W.; Mirin, N. A.; Nordlander, P. Plasmon Modes of Nanosphere Trimers and Quadrumers. *J. Phys. Chem. B* **2006**, *110*, 12302–12310.
47. Prodan, E.; Radloff, C.; Halas, N. J.; Nordlander, P. A Hybridization Model for the Plasmon Response of Complex Nanoparticles. *Science* **2003**, *302*, 419–422.
48. Urzhumov, Y. A.; Shvets, G.; Fan, J.; Capasso, F.; Brandl, D.; Nordlander, P. Plasmonic Nanoclusters: a Path towards Negative-Index Metafluids. *Opt. Express* **2007**, *15*, 14129–14145.
49. Mandel, L.; Wolf, E. *Optical Coherence and Quantum Optics*; Cambridge: Cambridge, U.K., 1995.
50. Hao, F.; Nordlander, P.; Burnett, M. T.; Maier, S. A. Enhanced Tunability and Linewidth Sharpening of Plasmon Resonances in Hybridized Metallic Ring/Disk Nanocavities. *Phys. Rev. B* **2007**, *76*, 245417.
51. Gersten, J.; Nitzan, A. Electromagnetic Theory of Enhanced Raman Scattering by Molecules Adsorbed on Rough Surfaces. *J. Chem. Phys.* **1980**, *73*, 3023–3037.
52. Liao, P. F.; Wokaun, A. Lightning Rod Effect in Surface Enhanced Raman Scattering. *J. Chem. Phys.* **1982**, *76*, 751–752.
53. Xu, H. X.; Bjerneld, E. J.; Aizpurua, J.; Apell, P.; Gunnarsson, L.; Petronis, S.; Kasemo, B.; Larsson, C.; Hook, F.; Kall, M. Interparticle Coupling Effects in Surface-Enhanced Raman Scattering. *Proc. SPIE* **2001**, *4258*, 35–42.
54. *COMSOL Multiphysics User's Guide*, version 3.3; Comsol Inc: Burlington, MA, 2006.
55. Lou, L.; Nordlander, P.; Smalley, R. E. Fullerene Nanotubes in Electric Fields. *Phys. Rev. B* **1995**, *52*, 1429–1432.
56. Dantzig, G. B. *Linear Programming and Extensions;* Princeton University Press: Princeton, NJ, 1963.
57. Taflove, A.; Hagness, S. C. *Computational Electrodynamics: The Finite-Difference Time Domain Method*; Artech House, Inc.: Norwood, MA, 2005.
58. Oubre, C.; Nordlander, P. Finite-Difference Time-Domain Studies of the Optical Properties of Nanoshell Dimers. *J. Phys. Chem. B* **2005**, *109*, 10042–10051.